PHYSICS OF PLASMAS **20**, 042502 (2013)

Jump conditions in transonic equilibria

L. Guazzotto,[1,a)] R. Betti,[1] and S. C. Jardin[2]
[1]*Department of Mechanical Engineering, University of Rochester, Rochester, New York 14627, USA*
[2]*Princeton Plasma Physics Laboratory, Princeton, New Jersey 08540, USA*

(Received 10 January 2013; accepted 11 March 2013; published online 2 April 2013)

In the present paper, the numerical calculation of transonic equilibria, first introduced with the FLOW code in Guazzotto *et al*. [Phys. Plasmas **11**, 604 (2004)], is critically reviewed. In particular, the necessity and effect of imposing explicit jump conditions at the transonic discontinuity are investigated. It is found that "standard" (low-β, large aspect ratio) transonic equilibria satisfy the correct jump condition with very good approximation even if the jump condition is not explicitly imposed. On the other hand, it is also found that high-β, low aspect ratio equilibria require the correct jump condition to be explicitly imposed. Various numerical approaches are described to modify FLOW to include the jump condition. It is proved that the new methods converge to the correct solution even in extreme cases of very large β, while they agree with the results obtained with the old implementation of FLOW in lower-β equilibria. © *2013 American Institute of Physics*. [http://dx.doi.org/10.1063/1.4798514]

I. INTRODUCTION

Tokamaks are currently the most advanced experiments in the path to controlled nuclear fusion and the production of energy. Nevertheless, many challenges still need to be met, and many improvements are still required before tokamaks become a viable source of energy. One of the critical factors determining the performance of tokamak experiments is the energy confinement time, which needs to be larger than some critical value of the order of a second in order to reach the burning plasma regime, when the fusion energy output greatly exceeds the input. It is well known that energy transport in tokamaks is reduced in the so-called high-confinement mode of operation (H-mode),[1] and that the creation of the edge transport barrier is related to the presence of highly sheared rotation in the poloidal direction (the short way around the torus). The region of high velocity shear is also characterized by a high density gradient (commonly known as density pedestal). Recently, it was suggested that H-mode profiles may be related to the discontinuous velocity and density profiles that naturally form in a toroidal system when a sufficiently large (but continuous) source of poloidal momentum is inserted in the system.[2,3] The velocity and density discontinuities are related to the (discontinuous) so-called transonic equilibrium,[4,5] which is the only equilibrium allowed by ideal magnetohydrodynamics (MHD) when the poloidal velocity is faster than the poloidal sound speed ($C_{sp} \simeq C_s B_p/B$, where C_s is the sound speed, B_p is the poloidal field, and B is the total magnetic field) at the edge of the plasma and small in the plasma core. The MHD transonic discontinuity is a special case of a wider class of discontinuities existing in fluid- and magnetohydrodynamics, namely, contact discontinuities, in which there is no velocity normal to the discontinuity (as opposed to shocks). More precisely, since pressure, tangential magnetic field and velocity are discontinuous, the transonic discontinuity is a tangential discontinuity. The wide literature on discontinuities in fluid dynamics, and in particular on transonic flows, even though not strictly relevant to the present work, should not be forgotten. Interested readers are referred, for instance, to Refs. 6–9. Incidentally, it has been pointed out that transonic flows are unlikely to be related to internal transport barriers.[10]

The present paper deals with a specific aspect of the transonic equilibrium problem, namely, the physical jump condition that needs to be satisfied at the transonic discontinuity. Numerical results are obtained with the code FLOW.[5] The issue was not considered in previous work on transonic equilibria because it only affects the equilibrium profiles when the discontinuity is located in a high-beta region ($\beta = 2p/B^2$), a condition that is certainly not verified in experiments.[10] Nevertheless, it is appropriate to include the correct jump condition in transonic equilibrium calculations, even if results for all cases of experimental interest are only very marginally influenced by such jump condition. In the present paper, it is shown that transonic equilibria with the correct jump condition can be calculated numerically also in situations where the old FLOW algorithm cannot find the correct equilibrium.

The remainder of the paper is organized as follows. In Sec. II, the problem of transonic equilibrium is briefly described. In Sec. III, the details of the partial differential equation governing the equilibrium and of the new approaches introduced in this work are discussed. Two strategies for obtaining a correct numerical solution are described in detail, and compared with the "old" method of solution implemented in the original version of FLOW. Numerical results for a "tokamak" equilibrium (where both the old and the new algorithms converge to the same correct result) and of a high-beta, spherical torus equilibrium (where the old algorithm does not converge to the correct equilibrium) are presented in Secs. IV and V. A benchmark problem is examined in Appendix B.

[a)] Author to whom correspondence should be addressed. Email: luca.guazzotto@rochester.edu

1070-664X/2013/20(4)/042502/16/$30.00

II. THE PROBLEM OF TRANSONIC EQUILIBRIUM

A brief review of the problem of MHD equilibrium in the presence of macroscopic rotation, with particular reference to transonic equilibria, is given in the present section for the sake of completeness. A more detailed discussion is given in Refs. 4 and 5. The starting point for the analysis is the set of isotropic MHD equilibrium equations, completed by the low-frequency Maxwell equations

$$\nabla \cdot (\rho \underline{v}) = 0, \tag{1a}$$

$$\rho \underline{v} \cdot \nabla \underline{v} = \underline{J} \times \underline{B} - \nabla p, \tag{1b}$$

$$\underline{J} = \nabla \times \underline{B}, \tag{1c}$$

$$\nabla \times (\underline{v} \times \underline{B}) = 0, \tag{1d}$$

$$\nabla \cdot \underline{B} = 0. \tag{1e}$$

In Eqs. (1), $\underline{v}$ is the fluid velocity, $\underline{B}$ is the magnetic field, $\underline{J}$ is the plasma current, ρ is the density, p is the (isotropic) pressure, and μ_0 has been set to unity for ease of notation. By assuming axisymmetry, the following relations are immediately obtained:

$$\underline{B}_p = \nabla\psi \times \nabla\varphi, \tag{2}$$

$$\underline{v} = \frac{\Phi(\psi)}{\rho}\underline{B} + R^2\Omega(\psi)\nabla\varphi, \tag{3}$$

where $\underline{B}_p$ is the poloidal component of $\underline{B}$, ψ is the poloidal flux, and $\Phi(\psi)$, $\Omega(\psi)$ are free functions of ψ. Three additional free functions of ψ are given by the closure equation

$$\frac{p}{\rho^\gamma} = S(\psi), \tag{4}$$

and by taking components of Eq. (1). Namely, the $\nabla\varphi$ component of Eq. (1) gives

$$B_\varphi = \frac{1}{R}\frac{F(\psi) + R^2\Phi(\psi)\Omega(\psi)}{1 - \Phi^2(\psi)/\rho}, \tag{5}$$

while the $\underline{B}$ component gives the Bernoulli equation

$$\frac{1}{2}\left[\frac{\Phi(\psi)B}{\rho}\right]^2 - \frac{1}{2}[R\Omega(\psi)]^2 + \frac{\gamma}{\gamma-1}S(\psi)\rho^{\gamma-1} = H(\psi). \tag{6}$$

The $\nabla\psi$ component of Eq. (1b) gives the modified Grad-Shafranov (GS) equation, which is discussed in detail in Sec. III.

Given the five free functions of ψ introduced above (F, Φ, Ω, H, S), the equilibrium state is determined by solving the system formed by the algebraic Bernoulli equation and the partial differential equation (PDE) GS equation. The GS equation is solved for ψ, while the Bernoulli equation can be seen as an equation for either the plasma density ρ or the poloidal Afvénic Mach number Φ^2/ρ.[11] The crucial element for the calculation of transonic equilibria is in the fact that the Bernoulli equation has in general more than one solution (up to four in the most general case). The two solutions corresponding to the slowest poloidal velocities give velocities smaller than the poloidal Alfvén speed (i.e., $\Phi^2/\rho < 1$). The "slowest" solution corresponds to a poloidal velocity smaller than the so-called poloidal sound speed $C_{sp} = C_s B_p/B$, while the next solution is larger than C_{sp}. The two solutions can be coincident in a single point of the cross section. We conform here to the standard tokamak notation and use the poloidal sound speed as the relevant velocity in the plasma, even though one should more correctly refer to the poloidal magneto-slow velocity, which in cases of interest is very close to the C_{sp} introduced above (see, for instance, Ref. 12). In the rest of the paper, we will refer to velocities smaller and larger than C_{sp} as sub- and supersonic poloidal flows. A transonic equilibrium is an equilibrium in which a different root of the Bernoulli equation is chosen in different regions of the plasma, separated by some critical value of ψ. Since the density assumes two different values on the two sides of the critical surface, a radial (tangential) discontinuity, called the transonic discontinuity, is found in the density profile. Due to Eqs. (3)– (5), a discontinuity in the density also produces a discontinuity in plasma velocity, Mach number, pressure, and toroidal field. Where the two solutions of the Bernoulli equation are coincident (typically on the inner midplane) all profiles are continuous. At all other angular locations, plasma properties are discontinuous across the transonic surface. The size of the discontinuity depends on the angular distance from the point where the two solutions of the Bernoulli equation are coincident,[4] and is maximum ad the outer midplane. The poloidal flux ψ is continuous across the critical surface, but the poloidal field is discontinuous.

The presence of a discontinuity in some plasma properties requires that a set of jump conditions across the discontinuity be satisfied. In past numerical solutions,[5,13] no explicit jump conditions were enforced, but it was verified *a posteriori* that the numerical solutions satisfied the necessary conditions. The purpose of this work is to address in detail the issue of jump conditions, and to show the effect of explicitly enforcing the jump conditions in the numerical solution of the GS equation.

At least one additional subtlety exists in the calculation of transonic equilibria, namely, the presence of a small hyperbolic region around the point where the two solutions of the Bernoulli equation are coincident, see, e.g., Refs. 5 and 14. Based on physical arguments, it has been argued in the past (see, e.g., Ref. 5) that the two transitions from the elliptic to the hyperbolic regime and back from hyperbolic to elliptic are not going to produce any major modification of the results obtained by numerical codes solving transonic equilibria. The proper treatment of the transitions and associated singularity is the object of active research, and will be discussed in future work. The present work will focus on a specific aspect of the transonic equilibrium calculation, i.e., the analysis of the jump conditions across the discontinuity.

Section III addresses the numerical solution of the GS equation in the presence of discontinuities.

III. GRAD-SHAFRANOV EQUATION AND JUMP CONDITIONS

We now turn our attention to the PDE determining the poloidal magnetic flux in axisymmetric equilibria, i.e., the modified Grad-Shafranov equation. In calculations of MHD equilibrium with arbitrary flow, the modified Grad-Shafranov equation is usually written in the form given in Ref. 14:

$$\nabla\cdot\left[\left(1-\frac{\Phi^2}{\rho}\right)\left(\frac{\nabla\psi}{R^2}\right)\right] = -\frac{B_\varphi}{R}\frac{dF(\psi)}{d\psi} - (\vec{v}\cdot\vec{B})\frac{d\Phi(\psi)}{d\psi} - R\rho v_\varphi\frac{d\Omega(\psi)}{d\psi} - \rho\frac{dH(\psi)}{d\psi} + \frac{\rho^\gamma}{\gamma-1}\frac{dS}{d\psi}. \quad (7)$$

Other, equivalent forms exist in the literature, with most of the apparent differences due to nomenclature. The GS equation is derived through straightforward manipulations from the $\nabla\psi$ component of the momentum equation, Eq. (1b) (or more easily with a variational approach[15]). As mentioned in Sec. II, a correct solution of the system of Eqs. (6) and (7) in the presence of discontinuities must ensure that the appropriate jump conditions are satisfied. The correct jump condition to be applied at the transonic discontinuity is given by the Rankine-Hugoniot condition

$$\left[\!\left[p+\frac{B^2}{2}\right]\!\right] = 0. \quad (8)$$

Due to the fact that the discontinuity is a tangential discontinuity, the component of both magnetic field and plasma velocity normal to the discontinuity is identically zero, and thus, Eq. (8) is the only meaningful jump condition [Ref. 16, p. 172]. Comparing Eqs. (7) and (8), it is seen that Eq. (7) imposes

$$\left[\!\left[\left(1-\frac{\Phi^2}{\rho}\right)\frac{\nabla\psi}{R^2}\right]\!\right] = 0, \quad (9)$$

which is *not* equivalent to Eq. (8). Equation (9) is true because we assume all free functions to be continuous, and thus, the right hand side of Eq. (7) to be bounded. The correct form of Eq. (9) should read

$$\left[\!\left[\left(1-\frac{\Phi^2}{\rho}\right)\frac{\nabla\psi}{R^2}\right]\!\right] = Q, \quad (10)$$

where Q is some function to be determined. A straightforward manipulation of Eqs. (8) and (10) gives

$$Q = \frac{2S(\rho_L^\gamma-\rho_R^\gamma)+\left(\frac{F+R^2\Omega\Phi}{R}\right)^2\left[\left(\frac{\rho_L}{\rho_L-\Phi^2}\right)^2-\left(\frac{\rho_R}{\rho_R-\Phi^2}\right)^2\right]}{\left.\frac{\partial\psi}{\partial n}\right|_R+\left.\frac{\partial\psi}{\partial n}\right|_L} + \frac{1}{R^2}\left(\frac{\Phi^2}{\rho_L}\left.\frac{\partial\psi}{\partial n}\right|_L - \frac{\Phi^2}{\rho_R}\left.\frac{\partial\psi}{\partial n}\right|_R\right), \quad (11)$$

where the subscripts L and R refer to the two sides ("left" and "right") of the discontinuity (let "left" correspond to the plasma core for convenience), and the partial derivative of ψ with respect to n is the derivative normal to the discontinuity, proportional to the poloidal field (remember that ψ itself is continuous, but the poloidal field is discontinuous). Alternatively, one may want to express Q as a $Q(\rho,\psi)$, rather than $Q(\rho,\psi,\nabla\psi)$, by eliminating $\nabla\psi$ in Eq. (11) in favor of the total pressure P_0 (assumed known) at the location of the discontinuity

$$\frac{\partial\psi}{\partial n} = \sqrt{2R^2P_0 - \frac{(F+R^2\Omega\Phi)^2}{\left(1-\frac{\Phi^2}{\rho}\right)^2} - 2R^2S\rho^\gamma}. \quad (12)$$

In principle, one could add a term $\sim Q\delta(\psi-\psi_{crit})$ to the right hand side of Eq. (7) and enforce the correct jump condition that way (ψ_{crit} is the critical value of ψ, where the transonic surface is located). In practice, it seems preferable to use a form of the GS equation that automatically includes the correct jump condition, without the need for a singular term. This can be achieved by having the gradient of the total pressure appear in the equation. A straightforward manipulation of Eq. (22) of Ref. 4 allows us to write the GS equation as

$$\left(1-\frac{\Phi^2(\psi)}{\rho}\right)|\nabla\psi|^3R\nabla\cdot\left(\frac{\nabla\psi}{|\nabla\psi|R}\right) + R^2\nabla\psi\cdot\nabla P_{tot} + RB_\varphi^2\frac{\partial\psi}{\partial R} - \rho Rv_\varphi^2\frac{\partial\psi}{\partial R} = 0. \quad (13)$$

The explicit presence of the total pressure $P_{tot}\equiv p+B^2/2$ in the equation ensures that no discontinuity in total pressure will be allowed in a converged equilibrium. It is worthwhile to point out that the quantity inside the divergence operator is a unit vector normal to the magnetic surface, $\psi = const.$, divided by the major radius R. Since the normal to the transonic surface is in the same direction on both sides of the discontinuity (which is equivalent to saying that the poloidal field does not change direction) and R is a Cartesian coordinate smooth by definition, the resulting vector inside the divergence is continuous, and thus, no formally divergent contributions can arise from the divergence term in Eq. (13).

The disadvantage of Eq. (13) with respect to Eq. (7) is its high nonlinearity. The nonlinearity is handled in FLOW successive over relaxation (SOR) method by using the previous iteration to calculate $|\nabla\psi|$ where needed. More specifically, all $|\nabla\psi|$ terms in Eq. (13), including the one necessary to calculate the poloidal field in P_{tot} and all ψ derivatives outside the divergence operator are expressed using the old-iteration value of ψ. A second-order interpolation is used to evaluate half-grid values. Due to non-linearity, the new numerical solution converges considerably more slowly than the old FLOW scheme. Equation (13) is used only in a region near the transonic discontinuity, and Eq. (7) (which is correct everywhere except at the discontinuity) is used in the rest of the plasma, with a weighted-average transition between the two forms. The approach is needed because $|\nabla\psi| = 0$ on the magnetic axis, which makes the coefficient of the first term in the equation vanish on the magnetic axis, and because the numerical evaluation of gradients near the plasma edge is less accurate than inside the plasma. In the following, we will refer to this approach for solving the transonic equilibrium problem as "method I."

Another approach is to modify the Bernoulli equation in order to completely dispense with the discontinuity. This has the advantage of improving the convergence of the numerical solver in the transonic region (see Sec. V). Also, since in a physical system, the discontinuity will be replaced by a sharp transition (with a width that can be expected to be proportional to the ion Larmor radius if kinetic effects are invoked, or to the ion skin depth if two-fluids effects are considered, see, for instance, Ref. 17), introducing a finite width for the transonic layer has the additional benefit of producing a more physical result, even though the layer width is for now purely a numerical artifact and not yet evaluated based on any physical estimation. Even though there is no discontinuity in this method, we will still occasionally refer to the transonic region as to the transonic discontinuity, especially when comparing results obtained with this approach to results obtained with other numerical implementations. The procedure is as follows. The Bernoulli equation (6) at any point on the transonic surface $\psi = \psi_{crit}$ is satisfied by two different values of ρ, ρ_L and ρ_R. The values ρ_L and ρ_R depend on the angular location (e.g., $\theta = \theta_0$, where θ is any poloidal coordinate) of the point under consideration (and are identical on the inner mid-plane). Intermediate values of ρ $(\rho_R < \rho < \rho_L)$ never satisfy Eq. (6) at $\theta = \theta_0$. If Eq. (6) is replaced by an equation that admits as solution any value $(\rho_R < \rho < \rho_L)$ at $\theta = \theta_0$ and in some neighborhood of $\psi = \psi_{crit}$, then the density profile will be continuous, and no jump conditions will need to be explicitly enforced. This method is referred to as "method II" or "Gauss-modified algorithm" in the rest of this work. The details of the derivation and implementation are discussed in Appendix A.

Both methods will be used in the remainder of this work. The next logical step in the transformation of the Bernoulli-GS system is to use Eq. (A2) in the derivation of the GS equation. Since methods I and II already give satisfactory results, this was done only for benchmark purposes.

It is worthwhile to mention that different approaches are also possible. In particular, one could use the conservation form of Eq. (1b)

$$\nabla \cdot \left[\rho\underline{vv} + \left(p + \frac{B^2}{2}\right)\underline{I} - \underline{BB}\right] = 0, \tag{14}$$

($\underline{I}$ is the identity tensor) and integrate it on a volume around the transonic discontinuity to obtain a relation between the values of ψ on the two sides of the discontinuity. This approach was considered, but discarded at least for the time being, since it would require major changes in the existing FLOW code.

A more promising possibility is to use flux coordinates in the solution of the GS-Bernoulli system. This requires to implement Eq. (7) in a flux coordinate system in a numerical solver, and to use a special treatment at the discontinuity. The advantage of this approach is that the discontinuity is located on a flux surface, i.e., on a curve aligned with one of the grid coordinates. Therefore, imposing the jump condition, Eq. (8) reduces to a one-dimensional problem. One can then set a grid point (in the ψ direction) on the discontinuity, and calculate the required gradients with a one-sided finite-difference scheme. As for the density, it is possible to define the density to be multi-valued on the critical surface, or to use a staggered grid for density and magnetic flux.

Since no specific choice was made for a system of coordinates in deriving Eq. (7), Eq. (7) is written in arbitrary coordinates. Therefore, in order to write the modified GS equation in flux coordinates, it is sufficient to express the differential operators in Eq. (7) in the appropriate system of coordinates. If a coordinate system (s, χ, φ) is used, where s is a flux label, χ is a poloidal angle, and φ is the toroidal angle, such that $\nabla s \times \nabla\chi$ is parallel to $\nabla\varphi$, one can simply take the well-known expressions for differential operators in flux coordinates (see, for instance, Ref. 18, p. 136) and replace

$$\nabla \cdot \left[\left(1 - \frac{\Phi^2}{\rho}\right)\left(\frac{\nabla\psi}{R^2}\right)\right] = \frac{1}{\mathcal{J}}\left[\psi'|\nabla s|^2\frac{\mathcal{J}}{R^2}\left(1 - \frac{\Phi^2}{\rho}\right)\right]_s + \frac{1}{\mathcal{J}}\left[\psi'\nabla\chi\cdot\nabla s\frac{\mathcal{J}}{R^2}\left(1 - \frac{\Phi^2}{\rho}\right)\right]_\chi, \tag{15}$$

where $\mathcal{J}$ is the Jacobian of the system of coordinates and $\psi' = \frac{d\psi}{ds}$ (of course $\psi' = 1$ if $s = \psi$). This approach was tested (in both staggered and non-staggered flavors) on a one-dimensional model problem described in Appendix B, using the fact that in the cylindrical case $s = r$, $\chi = \theta$, and derivatives with respect to θ are identically 0. Results were satisfactory, and thus, this method is still being considered for future versions of FLOW.

We now turn our attention to results obtained from the numerical solution of the GS equation described in the present section. In Secs. IV and V, results are given for a "standard" transonic equilibrium and for a high-β spherical torus (ST).

IV. TOKAMAK RESULTS

We start our discussion of results by examining equilibrium profiles calculated with the old and new implementations of FLOW for a "standard" transonic equilibrium. By

TABLE I. Main parameters of equilibria in Secs. IV and V.

Parameter	Tokamak value	ST value
Major radius	1.69	0.89
Minor radius	0.6	0.6
Average inverse aspect ratio	0.44	0.84
Ellipticity	1.6	1.6
Upper triangularity	0.5	0.3
Lower triangularity	0.4	0.5
Plasma current (kA)	673	671
Toroidal beta	9.6×10^{-3}	0.22

"standard" it is meant that this equilibrium is similar to the ones that have been published in the past when discussing transonic equilibrium, in the sense that the transonic discontinuity occurs near the plasma edge where pressure and temperature are small, and that numerically calculated poloidal velocities are of the order of ~10 to a few 10 s of km/s, i.e., in a range that is not unrealistic for experiments. The equilibrium considered in this section is based on an experimental low-β DIII-D equilibrium, to which transonic poloidal rotation was added. A non-symmetric plasma shape was chosen to emphasize the fact that plasma shape bears no influence on existence and qualitative properties of the transonic discontinuity. The main plasma properties are similar to the ones of the equilibrium used in Refs. 2, 3, and 19, and are listed in Table I together with the properties of the spherical tokamak equilibrium described in Sec. V.

The maximum poloidal velocity obtained in this equilibrium is $\simeq 33.7\,\mathrm{km/s}$. In all figures in this section, a reference equilibrium computed with the old implementation of FLOW on a 256×256 points grid and equilibria obtained with the new implementation and varying resolutions are compared in one-dimensional plots along the midplane. All results shown in this section were obtained using method I (no modification to the Bernoulli equation).

Results are shown in Figs. 1–3. First, we consider the poloidal flux and plasma density profiles shown in Fig. 1. To the scale of the plots, the results are indistinguishable: $|\psi_{old} - \psi_{new}|/\psi_{old} \sim 10^{-4}$ (in FLOW $\psi = 0$ on the plasma boundary). Incidentally, the two methods give slightly different results even for static equilibria, where no jump conditions need to be satisfied and where both Eqs. (7) and (13) are valid everywhere in the plasma. The position of the magnetic axis is identical. The "double maximum" density profile is due to the experimental profile used in the input. The discontinuity itself is located at $R \simeq 2.21$ m. The sharp density profile on the inner midplane is also due to the input experimental profile used for the density. The sharp, but continuous, profile in the inner midplane should not be confused with the discontinuous profile at the transonic discontinuity. The poloidal field B_p is presented in Fig. 2. As expressed by Eqs. (8) and (9), the poloidal field will have a variation across the transonic discontinuity that depends on the jump conditions imposed in the two different implementations. The value of B_p on the two sides of the discontinuity depends on the numerical scheme adopted for calculating the poloidal field. Centered differences over two grid cells are used in the present work. The results obtained with the old and new implementations hardly show any difference. Four different resolutions are used in Fig. 2 for the new implementation (FLOW requires a number of points that is a power of 2). All profiles match each other very closely, proving that the shown results correspond to a converged equilibrium solution. Only very close to the discontinuity, it is possible to observe a slight quantitative difference between the old and new results (box in the left bottom corner of Fig. 2). The relative difference between old and new values on the supersonic side of the discontinuity is $|B_p^{old} - B_p^{new}|/B_p^{new} \simeq 5 \times 10^{-3}$. The total pressure resulting from the old and new approaches (in atmospheres) is shown in Fig. 3. Only the region close to the transonic surface is shown, since the plots are once more all very close to each other. The total pressure is calculated using the poloidal fields shown in Fig. 2. As observed for the poloidal field, also the total pressure profiles only differ by very small amounts. The relative difference between old and new values on the supersonic side of the transonic discontinuity is $\sim 6 \times 10^{-4}$.

Since the difference between the results of the old and new implementation (using method I) appears to be very small, we do not investigate the issue any further, and do not deem necessary to also use method II for the tokamak equilibrium considered in this section. The smallness of the error in the old implementation (and its immediate consequence, that is the fact that the pressure profile appears to be smooth) is what prevented authors working on the numerical calculation of transonic discontinuities from recognizing the issue.

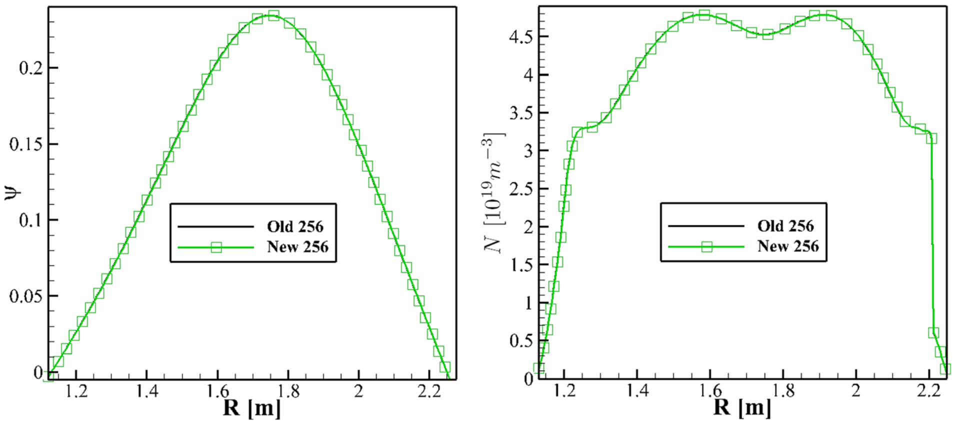

FIG. 1. Magnetic flux ψ (left) and number density (right) along the midplane, obtained with old and new implementation. Both old and new equilibria are calculated with a resolution of 256 points in each direction. Old and new results are to all practical purposes identical. The transonic discontinuity is at $R \simeq 2.21$.

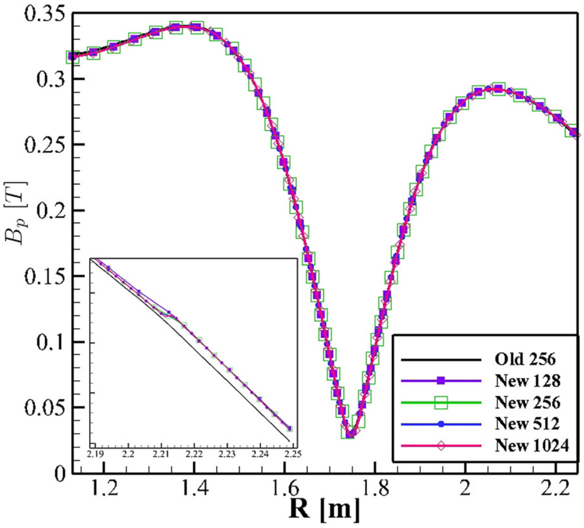

FIG. 2. Poloidal field along the midplane, obtained with the old and new implementation. Four different resolutions are used for the new implementation. Old and new results are to all practical purposes identical. The only difference is found near the transonic discontinuity at $R \simeq 2.21$ (shown in the lower left corner pane).

In a way, this is both fortunate and unfortunate. On the one hand, numerical results presented in the past for transonic equilibria are numerically correct up to negligible modifications. On the other hand, the lack of a numerically correct treatment of the physical jump condition, Eq. (8) has long remained unnoticed.

V. HIGH-BETA SPHERICAL TORUS RESULTS

We now repeat the analysis of Sec. IV, but using an equilibrium where we expect that not imposing the correct jump condition across the transonic discontinuity may have a non-negligible effect. This is done by assigning an input with large pressure near the transonic discontinuity. The equilibrium is based on an experimental high-β NSTX equilibrium of arbitrary shape, to which transonic poloidal rotation was added. The main equilibrium parameters are summarized in Table I. The maximum poloidal velocity in the equilibria in this section is in excess of 500 km/s. Clearly this is an unrealistic value: we stress the point that the equilibrium analyzed in this section is not an attempt to model any realistic equilibrium, but a numerical experiment to verify the accuracy of FLOW numerical solutions in a regime far beyond what is of experimental interest. The plots in the remainder of this section are used to highlight the similarities and differences between results obtained with the old and new implementations. In all figures, a reference equilibrium computed with the old implementation of FLOW on a 256 × 256 points grid and equilibria obtained with the new implementation and varying resolutions are shown. One-dimensional plots along the midplane are used for all figures. First, we present results obtained with method I in Figs. 4–7.

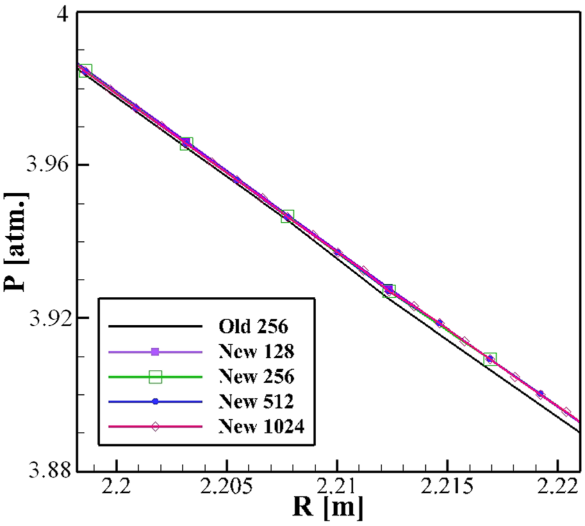

FIG. 3. Total pressure $P_{tot} = B^2/2 + p$ along the midplane, obtained with old and new implementation. Four different resolutions are used for the new implementation. Only the region near the transonic discontinuity at $R \simeq 2.21$ is shown, highlighting a minimal difference between the results of old and new implementation.

Magnetic flux and poloidal velocity are shown in Fig. 4. The results obtained for ψ are fairly similar: ψ_{axis} is $|\psi_{old} - \psi_{new}|/\psi_{old} \simeq 1.2\%$. The radial position of the magnetic axis obtained with a resolution of 256 × 256 points differs by one grid point between old and new implementation ($\sim$5 mm). The edge poloidal velocity is unrealistically large (the curves actually extend to $\sim$1000 km/s, or $\gtrsim$50 times the velocities we would expect from experimental measurements for a realistic equilibrium). All results are very close in the subsonic part of the plasma and in the inner midplane region. The profiles obtained with the new implementation are rather close to each other also near the transonic discontinuity, but there is a visible difference between old and new implementation. The old implementation finds a slightly different position for the transonic surface and a smaller velocity in the supersonic region (see zoom of the transonic region, top left part of the velocity plot in Fig. 4). We observe that the solution of the new implementation is converging, as all profiles are located in the same position and V_p values are almost identical where the grid points overlap, while the discontinuity is becoming sharper with increasing resolution. The poloidal field is shown in Fig. 5 (a zoom of the transonic discontinuity region is presented on the right). Plots only differ close to the discontinuity region and in the supersonic region. The new implementation gives a large jump in the poloidal field, which is missed by the old one, which however correctly identifies the change in slope of B_p. In producing the plots in Fig. 5, we chose again to use the simplest numerical approach, i.e., centered finite differences (keep in mind that B_p is a derived quantity, calculated by a post processor). The result of this choice is that the poloidal field in the grid points closest to the discontinuity is not calculated correctly. However, since the field calculated in grid points that do not require to differentiate across the discontinuity are accurate, we will still be able to see the finite variation of B_p across the discontinuity. Simply, instead of a jump between two adjacent grid points our post-processor will produce a transition over three grid points. From the right part of Fig. 5, it is seen that the new implementation converges to a true discontinuity with increasing number of points, with the numerical values of the field on the two sides of the

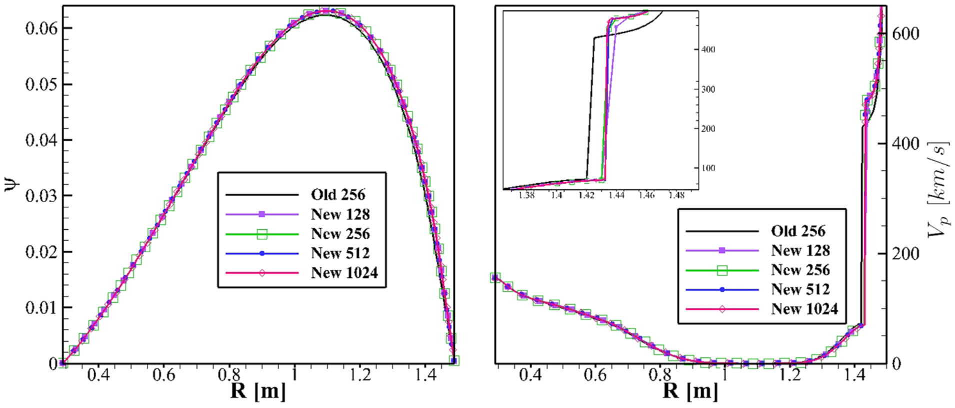

FIG. 4. Magnetic flux ψ (left) and poloidal velocity in km/s (right) along the midplane obtained with old and new implementation (method I). Results for ψ are all very close (with some difference between old and new implementation). Poloidal velocities are also very close in most of the plasma, with a visible difference only around the transonic discontinuity. The box on the top left shows a zoom of the transonic discontinuity region.

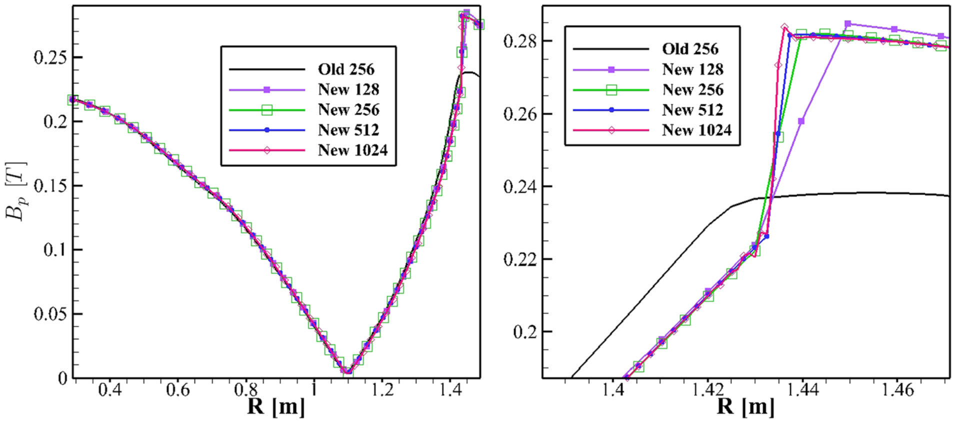

FIG. 5. Poloidal field along the midplane. All results are rather similar everywhere except in the supersonic zone at large major radius (i.e., in the area near and outside the MHD pedestal). The left pane shows the complete midplane profiles and the right pane a zoom of the transonic discontinuity.

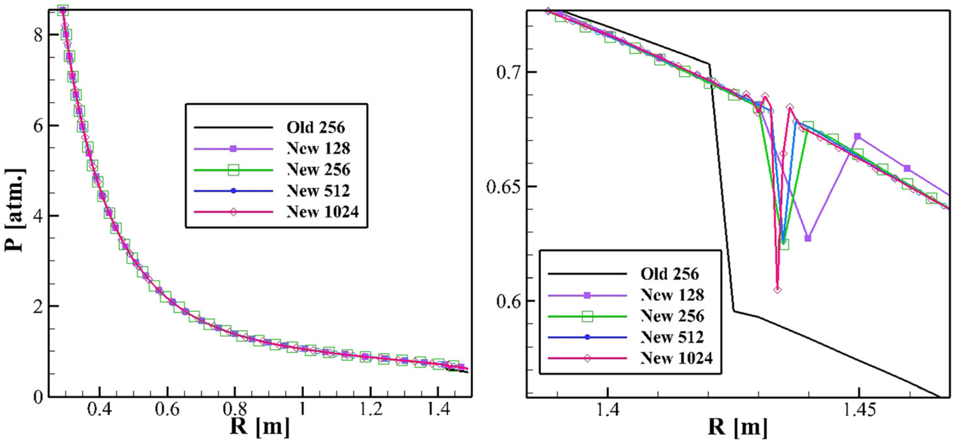

FIG. 6. Total pressure $p + \frac{B^2}{2}$ as a function of R along the midplane (left) and zoom of the transonic discontinuity region (right). All profiles are very similar in the part of the plasma inboard of the transonic discontinuity. A discrepancy between the new and old implementation is visible in the lower right hand corner of the figure. For consistency, all profiles are calculated in the same way, with centered differences for the poloidal field.

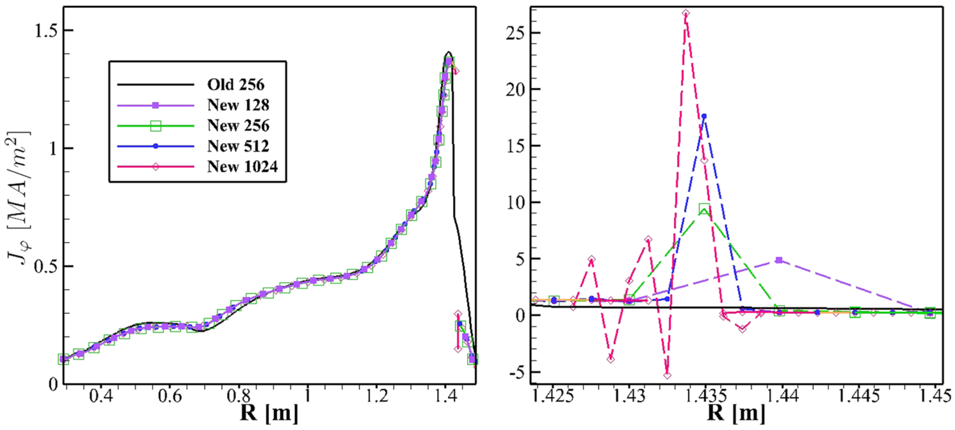

FIG. 7. Toroidal current J_φ along the midplane. The total profile is shown on the left, and a zoom of the transonic region on the right. Large peaks are obtained across the discontinuity, with height increasing and width decreasing with increasing number of grid points. On the left, the transonic region is not plotted for the new implementation for clarity. Oscillations are present in and around the transonic region. The current is calculated with Eq. (16) (dashed lines) and with Eq. (17) (continuous lines).

discontinuity being essentially identical for all resolutions. Some small oscillations, which we consider to be of numerical origin, appear in the equilibrium with the highest resolution. In fact, the appearance of oscillations near the transonic surface in method I was one of the reasons why method II was introduced: Since there is no discontinuity in method II, we expect a smoother numerical solution and no oscillations. We will examine later the results of method II. Notice that, as expressed by Eq. (3), the poloidal velocity depends directly on the poloidal field. The different values obtained for the poloidal field explain the difference in poloidal velocity between old and new implementation observed in Fig. 4. The effect of the density jump on the velocity jump is the same for the old and new implementations, since the density jump is almost identical in all numerical results, even though the position of the transonic discontinuity is slightly different between old and new results. Next we consider the total pressure $P_{tot} = p + B^2/2$, shown in Fig. 6.

The left part of the figure shows the pressure profile over the whole midplane and the right part of the figure a zoom of the transonic region. A clear difference between old and new implementations is found only in the supersonic region outboard of the transonic surface. All results obtained with the new implementation are very similar, once more confirming the convergence properties of the numerical solution. Some oscillations are again present in the profile with the highest resolution (see above). The old implementation produces a discontinuous profile, while the new one gives a smooth result. The presence of a "dip" in the profile is simply the effect of the way the poloidal field is calculated by the post-processor evaluating the total pressure (the same evaluation of B_p is used everywhere for consistency). It is important to emphasize that the total pressure shown in Fig. 6 is *not* the total pressure that is used in the inner workings of the numerical solution of Eq. (13) (which contains a ∇P_{tot} term). Indeed, the whole point of having a ∇P_{tot} term in the GS equation is to guarantee that P_{tot} be continuous. This is accomplished in the code by using an interpolation function and finite differences in a way that guarantees that P_{tot} is a continuous function.

The toroidal current density J_φ in shown in Fig. 7; the right part of the figure shows a zoom of the transonic discontinuity region. The large spike and accompanying oscillations of J_φ seen in the right part of the figure have been removed from the plot on the left to avoid confusion. Two different approaches can be used to calculate the current density profile. First, one can simply write a finite-difference numerical approximation of Ampère's law

$$J_\varphi = \hat{e}_\varphi \cdot \nabla \times \underline{B} = -R\nabla \cdot \frac{\nabla\psi}{R^2} \equiv -\frac{1}{R}\Delta^*\psi. \tag{16}$$

Another possibility is to use Eq. (7) and write

$$\nabla \cdot \frac{\nabla\psi}{R^2} = \frac{\mathcal{RHS} + \frac{1}{R^2}\nabla\psi \cdot \nabla\frac{\Phi^2}{\rho}}{1 - \frac{\Phi^2}{\rho}}, \tag{17}$$

where

$$\mathcal{RHS} = -\frac{B_\varphi}{R}\frac{dF(\psi)}{d\psi} - (\vec{v}\cdot\vec{B})\frac{d\Phi(\psi)}{d\psi} - R\rho v_\varphi \frac{d\Omega(\psi)}{d\psi} - \rho\frac{dH(\psi)}{d\psi} + \frac{\rho^\gamma}{\gamma - 1}\frac{dS}{d\psi} \tag{18}$$

is the right-hand side of Eq. (7). While the direct differentiation in Eq. (16) is valid everywhere, Eq. (17) can only be used where Eq. (7) is valid, i.e., everywhere except at the transonic discontinuity. Keep in mind that in the model of transonic discontinuous equilibrium, the poloidal field is discontinuous and the current density diverges at the transonic surface: This is reproduced by Eq. (16), but not by Eq. (17), which does not take the derivative of the poloidal field. The two approximations give very similar results where they are both valid (which should not be surprising, since in practice they correspond to the left- and right-hand sides of the GS equation). The usefulness of Eq. (17) is in the fact that its evaluation requires only first derivatives (as opposed to the second derivatives necessary for Eq. (16)), and thus, its results are more accurate and less prone to contain oscillations. In Fig. 7, results obtained with Eq. (16) are shown with dashed lines, and results obtained with Eq. (17) with continuous lines. All results (old and new with different resolutions) in Fig. 7 are quite similar everywhere except near the region of the transonic discontinuity. A large current spike across the discontinuity is found by the new implementation; the spike is completely missed by the old implementation. The spike becomes narrower and higher with increasing resolution. Large numerical oscillations appear in the equilibrium with the highest resolution. Small oscillations (not visible in Fig. 7) are also seen for the lower resolution equilibria.

The numerical results presented this far prove that transonic equilibria with high beta at the location of the discontinuity can be handled correctly by the numerical implementation introduced in Sec. III. It is now worthwhile to investigate if the additional modification to the Bernoulli equation of method II will have any positive effect on the numerical evaluation of the quantities of interest. In particular, one would expect that replacing a discontinuity with a sharp, but finite, gradient will at least ameliorate the issue with oscillations seen in Fig. 7. Also, the fact that everything (including the total pressure) is continuous by construction should result in smoother profiles for the total pressure. Additional reasons for introducing method II where given in Sec. III. The price to pay for introducing method II is that the discontinuity has been removed from the system, and thus, we are solving a simpler problem. It is proven in Appendix B that method II converges to the discontinuous solution in the limit of infinite grid resolution. We repeat the equilibrium calculation using method II, again with grid resolutions from 128 to 1024 points in each direction. Not surprisingly, most numerical results are very similar to the ones obtained with method I. In the remainder of this section, we will only show some representative numerical results. Incidentally, it is mentioned that the relative difference between the new and old values of ψ_{axis} is $\sim$2%, to be compared to the relative difference of $\sim$1.2% found with method I.

Results for method II are shown in Figs. 8–11. The poloidal field profile in the transonic region is shown in Fig. 8. No qualitative difference is found with respect to method I. In this case, calculating the poloidal field with a centered finite difference method does not introduce any additional approximation, since the profile is continuous, even though steep. The convergence of the method is seen in the identical values assumed by the poloidal field for all grids in the new implementation on the two sides of the discontinuity. The increasing poloidal field gradient with increasing resolution also shows the progressive reduction of the transonic layer width. Methods I and II give fairly similar results, but the poloidal field obtained with method II is slightly larger (also away from the transonic region, even though the difference in the part of the plasma inboard of the transonic surface is extremely small). The toroidal current profile in the transonic region, calculated with Eq. (16), is shown in Fig. 9. As was the case in Fig. 7, a current spike near the transonic surface is found, with height increasing and width decreasing for increasing resolution. Differently from Fig. 7, no large oscillations near the transonic surface appear at high resolution. Some oscillations are still present in equilibria with lower resolution. One clear feature of the profile is the sign change of J_φ after the transonic region. This effect is very localized and likely of numerical origin. The total pressure profile is shown in Fig. 10. Since method II replaces discontinuities with sharp gradients, P_{tot} is automatically continuous, and no "dips" such as those seen in Fig. 6 are found. In this case, some oscillations are present for the equilibrium with the lowest resolution (possibly due to a local convergence problem). The total pressure gradient has a sharp change across the transonic region (i.e., there is a clear change in slope in the P_{tot} profile). This is mostly due to the change in slope in B_p, which is seen in Fig. 8. The same general behavior is obtained with method I, even though the presence of the "dip" makes the effect less visible. The total pressure profiles obtained with methods I and II are very similar, with the profile obtained with method II being slightly larger (not shown). Density profiles obtained with method II are shown in Fig. 11, with zoom of the transonic region in the right part of the figure. All profiles look quite similar everywhere, even though the position of the transonic discontinuity is slightly shifted with respect to the one found by the old method. What is remarkable (and exactly as foreseen) is the fact that the density profiles in Fig. 11 are indeed smoother. This can be noticed comparing

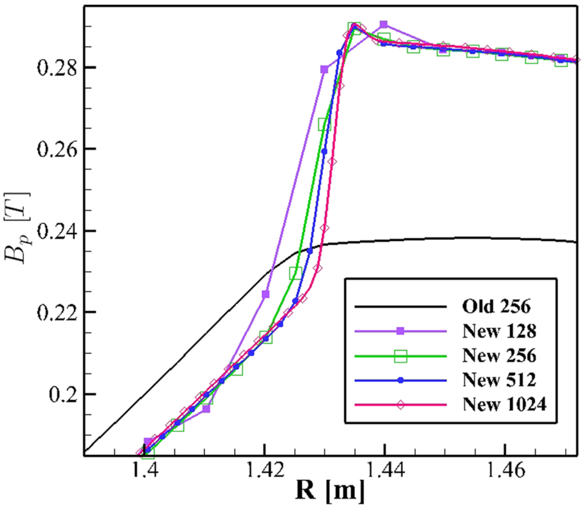

FIG. 8. Zoom of the discontinuity region for the poloidal field profile along the midplane. The sharp variation of B_p in the new implementation, as opposed to the smooth profile of the old one, is visible. The variation of B_P becomes steeper with increasing resolution.

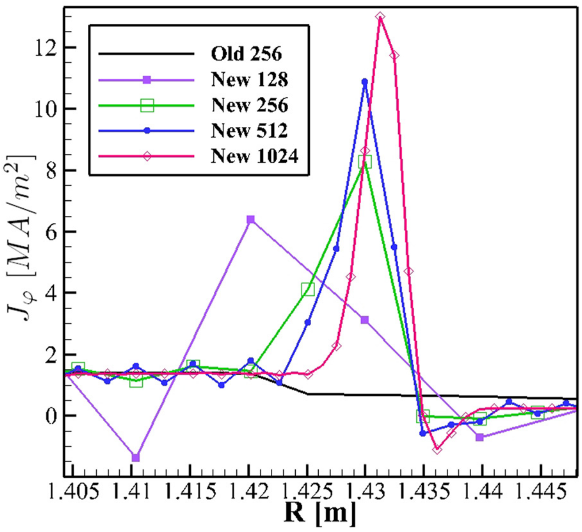

FIG. 9. Toroidal current along the midplane for the old and "Gauss-modified" algorithms. The appearance of a current density spike is observed. The spike height increases with increasing resolution. Some small numerical oscillations are still seen in the profiles obtained with the new algorithm, but disappear with high resolution. The current reversal by the transonic discontinuity is likely numerical. Observe that the spike is lower than the one obtained with the other new algorithm, but also wider. Results are calculated with Eq. (16).

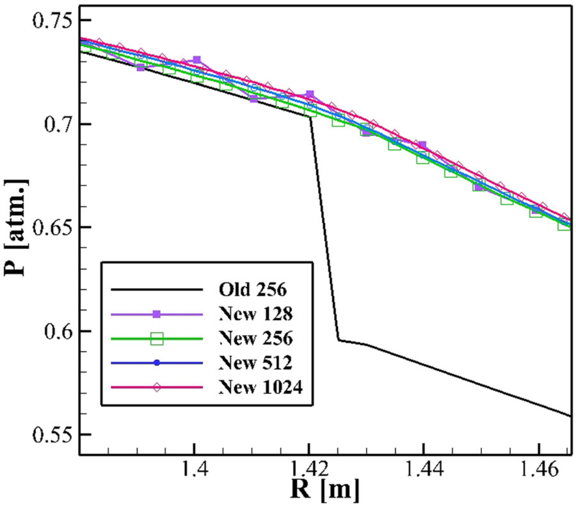

FIG. 10. Total pressure along the midplane for the "Gauss-modified" algorithm (limited to the region of the transonic discontinuity). The profiles obtained with the new implementation are continuous and smooth (barring some slight oscillation in the one with lowest resolution). Also, the gradient of the total pressure changes across the discontinuity. This is consistent with the results of method I (compare with Fig. 6), but the plot is more clear due to the consistent representation for the total pressure used in the diagnostic and the internal evaluation of the total pressure gradient.

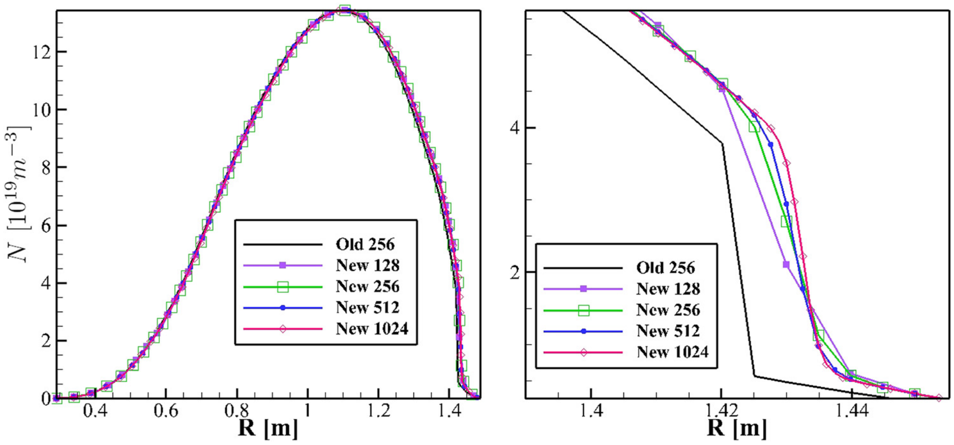

FIG. 11. Density profile along the midplane for the old and "Gauss-modified" algorithms. All profiles are quite similar everywhere. Zoom of (density profile) restricted to the region of the discontinuity. The steepening of the profile with increasing resolution is visible. The position of the transonic discontinuity is slightly shifted with the new implementation. Comparing the new curves with the old one, it is seen that the new algorithm spreads the discontinuity over ~4 grid points (the slopes of the new curve with 1024 points is about the same as the old one with 256 points).

the old and new profiles with 256 grid points. One additional point that can be made from Fig. 11 is the fact that method II spreads the discontinuity on approximately 4 grid points (with the value of Δ used in the calculations presented here, see Appendix A for the definition of Δ). This is recognized by observing that the steepness of the old (discontinuous) profile calculated with 256 points is approximately the same of the one obtained with the new method with four times as many points.

VI. CONCLUSIONS AND DISCUSSION

In this work, a critical reevaluation of the numerical solution of transonic equilibria was presented. The analysis was inspired by the fact that until now the physical jump condition given by Eq. (8) was not explicitly enforced in any of the codes capable of calculating transonic equilibria. It was verified in the past that the correct jump condition is satisfied by the codes with excellent numerical approximation if realistic profiles are used (in particular with reference to plasma beta and poloidal velocity). It was found that the numerical solution of the code FLOW is not correct across the discontinuity for (unrealistic) profiles specifically designed to produce discontinuities with large beta and poloidal velocity. Two ways to fix the numerical solver were introduced. First, it is possible to write a modified Grad-Shafranov equation that automatically satisfies the physical jump conditions. This comes at the price of a high nonlinearity in the differential operator, which severely slows down the numerical solver. Another possibility is to remove the discontinuity, by spreading it over a finite region through a modification of the Bernoulli equation. This method is used in conjunction with the previous one, since it still requires to solve the modified version of the GS equation. Its beneficial effect is mainly in the reduction of oscillations near the transonic region. One final possibility is to modify the original form of the GS equation with flow to consistently include the effect of a sharp variation across the transonic region. This was used only for benchmark and is discussed in Appendix C. Numerical calculations with the "new" implementations show that the physical jump conditions are correctly reproduced by FLOW, even in the presence of very large discontinuities.

It is worthwhile to consider the Mach number profiles shown in Fig. 12 to emphasize the difference between the two methods presented in Sec. V for correctly solving the equilibrium problem across the transonic region. The Mach number is defined as $M = v_p/C_{sp}$. While both methods satisfy the correct jump condition, method I is solving the discontinuous problem, and method II is solving a regularized version of the problem, with no discontinuities. Thus, as expected from the theory, the Mach number profile is smooth for both methods at the inner midplane, Fig. 12(a), since in both methods the Bernoulli equation has two coincident solutions at the inner midplane. The inner midplane is the only region in which method I gives a smooth profile, since a discontinuity (due to the difference between the two solutions of the Bernoulli equation) is present at any other angular location. The profile in method II is flatter near $M = 1$ because the modification of the Bernoulli equation makes the two solutions of the equations very close to each other in a small region around the transonic surface. Strictly speaking, the transition between "subsonic" and "supersonic" flows occurs for M slightly less than unity. In the outer

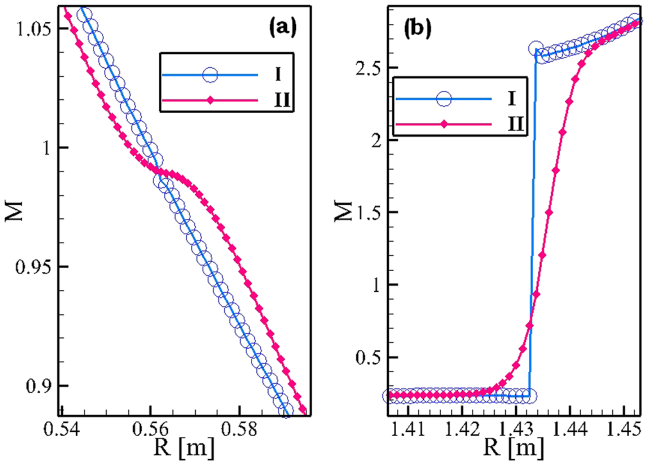

FIG. 12. Mach number profile across the transonic region at the inner (a) and outer (b) midplane for the ST equilibrium in Sec. V with methods I and II. Both profiles are continuous at the inner midplane, while the profile obtained with method I is discontinuous at the outer midplane. Notice the different scale on the vertical axis in the two parts of the figure.

midplane, method I gives a true discontinuity, while method II has a smooth profile. Notice the different vertical scale in the two parts of the figure. Each symbol corresponds to a grid point.

In practice, the difference between old and new results for realistic profiles is such as to be entirely negligible for equilibrium calculations. One may wonder whether any effect will appear on the stability of transonic equilibria depending on the implementation of the correct jump conditions at the discontinuity. Since no stability calculations for transonic equilibria are available to date, we turn the question into a simpler one, and try and compare safety factor (q) profiles for the old and new implementations. Once again, up to the resolution considered in the present work, no appreciable difference is seen in the tokamak case of Sec. IV. However, a clear, even though limited to the transonic region, difference is observed for the ST equilibrium discussed in Sec. V. This is shown in Fig. 13, where the safety factor profile obtained with the old FLOW implementation and a grid of 256 points (black curve) is compared to the profile obtained with the new implementation and method II with a resolution of 1024 points (red curve, symbols). Curves are shown along the midplane versus the major radius. The two plots are almost identical everywhere, except near the transonic region. Around the transonic discontinuity, due to the discontinuity in the poloidal field (see, e.g., Fig. 8), the safety factor also changes rapidly. In Fig. 13, the magnetic shear reversal at the transonic surface is evident. For completeness, it needs to be mentioned that the q profiles shown in Fig. 13 were calculated with a numerical integration of the q profile definition on a number of magnetic surfaces $\sim N/3$, where N is the number of grid points in each Cartesian direction. Since the grid used by FLOW is not aligned with the magnetic surfaces, quadratic interpolations were used to evaluate the magnetic field on the flux surfaces. One should also keep in mind that the q profile is sensitive to the method used to enforce the jump conditions (since method II actually spreads the discontinuity over a finite range). Thus, the result highlighted by Fig. 13 is not a completely conclusive result, but rather a qualitative indication of the fact the fine detail of the safety factor profile in the transonic region is modified by the presence of a transonic discontinuity. Even though more work will be needed to obtain more accurate results, a qualitative difference (flattening or reversal of the q profile) is identified in the present work. Two elements should be added to our calculation for a more accurate evaluation of the safety factor profile: First, the grid should be aligned with the magnetic surfaces, second, a physics-based approach should be used to resolve the transonic discontinuity predicted by ideal MHD. The first point is under consideration for future versions of FLOW. The second one is being developed: the next step in transonic equilibrium calculations will be the use of a two-fluid model, in which we expect the transonic discontinuity to acquire a width of the order of the ion skin depth.[17] Future results will give a further improvement of the model and understanding of transonic equilibria.

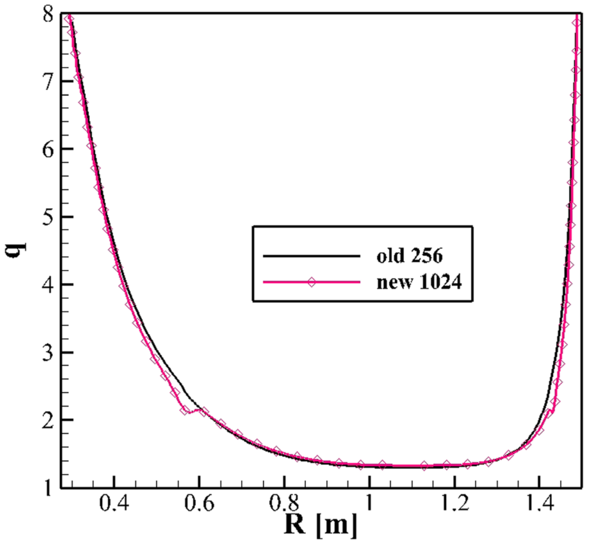

FIG. 13. Safety factor profile for the high-β ST equilibrium in Sec. V. The old (black curve) and new (red curve, diamonds) agree very well in most of the plasma, but the new curve shows a reversal of the magnetic shear in the transonic region.

ACKNOWLEDGMENTS

The authors thank H. Weitzner for first pointing out the issue in the numerical solution of transonic equilibria and E. Hameiri and R. Keppens for useful discussion. One of the authors (L.G.) gratefully acknowledges PPPL for its continuing hospitality during the preparation of this work. This work was supported by the U.S. Department of Energy under Contract No. DE-FG02-93ER54215. Partial financial support was provided by Marie Curie Grant PIRG-GA-2009-256385.

APPENDIX A: DISCONTINUITY REMOVAL BY MODIFICATION OF BERNOULLI EQUATION

We start by defining for convenience

$$\mathcal{B}(\rho;\psi) = \frac{1}{2}\left[\frac{\Phi(\psi)B}{\rho}\right]^2 - \frac{1}{2}[R\Omega(\psi)]^2 + \frac{\gamma}{\gamma-1}S(\psi)\rho^{\gamma-1} - H(\psi). \tag{A1}$$

Next, the Bernoulli equation is modified to

$$\frac{1}{2}\left[\frac{\Phi(\psi)B}{\rho}\right]^2 - \frac{1}{2}[R\Omega(\psi)]^2 + \frac{\gamma}{\gamma-1}S(\psi)\rho^{\gamma-1} = H(\psi) - f, \tag{A2}$$

where f is defined by

$$f = f_0 e^{-\Delta\left(\frac{\psi-\psi_{crit}}{\psi_c}\right)^2} \tag{A3}$$

(ψ_c is the maximum value of ψ in the plasma, which in our notation corresponds to the magnetic axis). The value f_0 is determined by

$$f_0 \equiv \mathcal{B}(\rho_0;\psi), \tag{A4a}$$

and ρ_0 is defined by

$$\frac{\partial \mathcal{B}(\rho_0;\psi)}{\partial \rho} = 0. \tag{A4b}$$

In a more descriptive way, at any given point, we keep ψ fixed and find the value of ρ that maximizes the Bernoulli function. Then the maximum value of the Bernoulli equation is calculated, and added to the Bernoulli equation with an exponential dependence on ψ. It is easy to verify that this additional term replaces the discontinuity obtained from the Bernoulli equation with a smooth transition through a layer, the thickness of which is controlled by the parameter Δ. In the following, Δ is set to be proportional to N (N is the number of grid points), giving a decreasing layer width with increasing number of points. For the numerical solution of the equilibrium, we remark that the new Bernoulli equation (A2) always has a single sub-Alfvénic solution for $\psi = \psi_{crit}$, and two separate solutions if $\psi \neq \psi_{crit}$. As is done in the usual transonic equilibrium calculations, the largest root is chosen in the subsonic part of the plasma, and the smallest one in the supersonic region. The two roots of Eq. (A2) are closer to each other than the roots of Eq. (6), and the more so the closer one gets to the transonic surface. This clarifies how using Eq. (A2) instead of Eq. (6) replaces the discontinuity with a smooth transition.

It is now necessary to verify what changes are necessary in the other equilibrium equations due to the modification of the Bernoulli equation. As discussed in Sec. II, the equilibrium equations (5)–(7) and (13) are obtained by taking components of Eq. (1). It is then natural to modify Eq. (1) by adding a fictitious force $\underline{\mathcal{F}}$ that produces the required modification in Eq. (6) to give Eq. (A2)

$$\rho \underline{v} \cdot \nabla \underline{v} = \underline{J} \times \underline{B} - \nabla p + \underline{\mathcal{F}}. \tag{A5}$$

Ideally, one would prefer $\underline{\mathcal{F}}$ not to have any effect on the definition of the toroidal field (the $\nabla\varphi$ component of the momentum equation) and on the normal force balance (the $\nabla\psi$ component). Formally, this translates to the set of equations

$$\nabla\varphi \cdot \underline{\mathcal{F}} = 0, \tag{A6a}$$

$$(\nabla\psi \times \nabla\varphi) \cdot \underline{\mathcal{F}} = (\nabla\psi \times \nabla\varphi) \cdot (\rho \nabla f), \tag{A6b}$$

$$\nabla\psi \cdot \underline{\mathcal{F}} = 0, \tag{A6c}$$

where f is given by Eq. (A3). A trivial solution is found by writing

$$\underline{\mathcal{F}} = \rho\left[\nabla f - \frac{\nabla f \cdot \nabla\varphi}{|\nabla\varphi|^2}\nabla\varphi - \frac{\nabla f \cdot \nabla\psi}{|\nabla\psi|^2}\nabla\psi\right]. \tag{A7}$$

This allows us to consistently leave toroidal field and normal force balance unchanged after the introduction of $\underline{\mathcal{F}}$. One slight subtlety that still needs to be taken into account is that in deriving Eq. (7), it is necessary to substitute the gradient of the left hand side of Eq. (6) with the gradient of the right hand side of the same equation (this is what makes the derivative of H appear in Eq. (7)) during the derivation, while that is not the case for Eq. (13). Incidentally, this is the reason why Eq. (7) is not valid across the discontinuity, since in order to derive it one needs to take derivatives of functions that are discontinuous across the transonic discontinuity. Therefore, Eq. (13) should still be used in conjunction with Eq. (A2). Equation (7) can still be used far from the transonic surface, where the new term f in Eq. (A2) is negligible. It may look at this point as if the modification of the Bernoulli equation did not bring any real benefit, since it will still be necessary to solve the same differential equation that was used for method I and face the same numerical difficulties. In fact, there is a clear advantage in the solution of the system of Eqs. (6) and (13) with respect to method I, because there are no discontinuities in method II, and therefore, there is no need for any special treatment of the ∇P_{tot} term in Eq. (13), since P_{tot} is automatically continuous.

APPENDIX B: ONE-DIMENSIONAL BENCHMARK

Having examined in detail the problem of transonic equilibria in toroidally symmetric systems in various conditions, it is useful to verify the convergence properties of the numerical solution for some benchmark problem. The approach is to calculate transonic equilibria for a cylindrical system, i.e., a one-dimensional system, which can be approximated by FLOW using a high aspect ratio. The cylindrical equilibrium is entirely determined by the radial force balance. However, it is also possible to express the same problem in a Grad-Shafranov-like form, see, for instance, Ref. 20 where various symmetries, in particular, the translational one corresponding to cylindrical equilibria, are introduced to simplify the equilibrium system given by Eqs. (1). With this approach it becomes trivial to assign the same input to the one- and two-dimensional systems, and thus, make a meaningful comparison.

In the one-dimensional equilibrium a grid point can be set on the discontinuity, and Eq. (8) is enforced exactly at the location of the transonic discontinuity. This is done by imposing the radial force balance

$$\frac{d}{dr}\left(p + \frac{B^2}{2}\right) + \frac{B_p^2}{r} - \rho\frac{v_p^2}{r} = 0, \tag{B1}$$

at the location of the discontinuity, where gradients are calculated using one-sided approximations of all discontinuous quantities. For B_p and V_p, the average between the values on the two sides of the discontinuity is used. A staggered grid is used in the 1D problem, with the density being calculated at half grid point of distance from ψ. A boundary condition $\psi = 0$ is used at the edge ($r = 1$), and a parabolic extrapolation is used in $r = 0$. Regarding the transonic discontinuity, an arbitrary location ($r = 0.7$ in the equilibrium presented in this section) is selected to switch from the subsonic to the supersonic root of the Bernoulli equation. A slight subtlety is in the fact that in this case it is not necessary to adjust the free functions of ψ in order to make the two solutions of the Bernoulli equation coincident in one point of the transonic surface, as is instead done for the 2D problem (see the figures in Secs. IV and V). Indeed, since there is no θ dependence in the problem, making the two solutions coincident in one point would actually make them coincident over the whole transonic surface, and result in an equilibrium that is

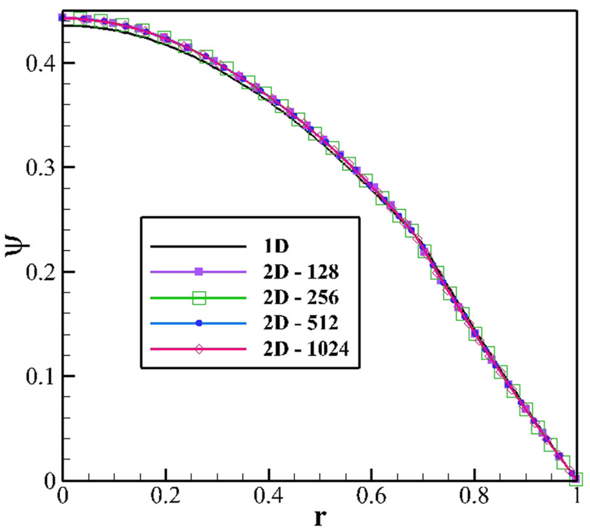

FIG. 14. Magnetic flux calculated with the 1D and 2D codes with different resolutions. All results show good agreement.

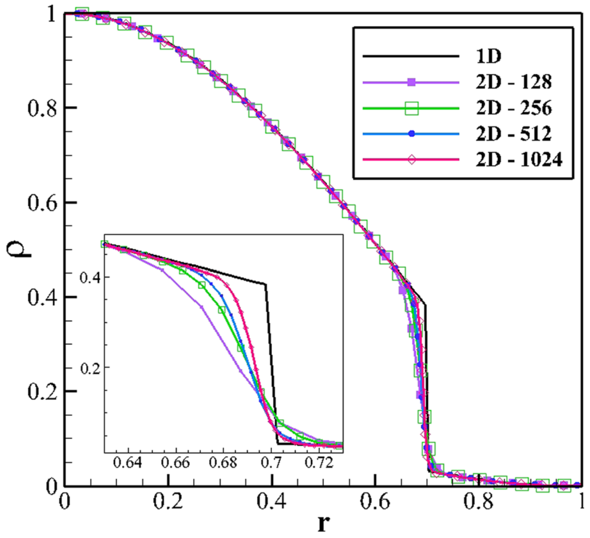

FIG. 15. Plasma density (in arbitrary units) calculated with the 1D and 2D codes with different resolutions. All results show good agreement. The inset in the left-bottom corner of the plot shows details of the profile near the transonic surface.

everywhere continuos. Simple, analytic shapes are chosen for all free functions. In order to make the effect of the transonic discontinuity very dramatic, a large beta is assigned in the plasma. At the location of the discontinuity the plasma beta jumps from $\simeq 0.45$ to $\simeq 4.5 \times 10^{-3}$. We intentionally selected a numerically very difficult problem (due to the large beta and large jump) in order to have a critical assessment of the properties of the new solver. Plots of various quantities for a reference equilibrium calculated with the one-dimensional solver and 400 grid points and for the new implementation of FLOW with various grid resolutions are presented in the remainder of this section (keep in mind that FLOW solves the complete circular cross section, not only the 1D problem with $0 < r < 1$). FLOW results are obtained assigning an aspect ratio of 10^3. Only method II (modification of Bernoulli equation in conjunction with the non-linear algorithm for Eq. (13)) was used for the results in this section. The same expression for Δ in Eq. (A3) that was used in Sec. V is used here.

First we examine the magnetic flux profile, shown in Fig. 14. All two-dimensional equilibria are very close to each other, and also fairly close to the one-dimensional one. In particular, the change in slope at $r = 0.7$ (the location of the discontinuity) is visible in all equilibria. The peak value of ψ obtained with the two-dimensional solver is slightly larger ($\sim$1.6%.) than the value calculated with the 1D approach. In order to make a meaningful comparison, the two-dimensional results were divided by the major radius $R_0 = 10^3$.

The next plot, Fig. 15, shows the density profile (in arbitrary units) obtained with the 1D solver and with FLOW using resolutions between 128 and 1024 points. A zoom of the transonic region is included at the bottom left corner of the figure to give more details on the accuracy and convergence of the FLOW solutions. All profiles align rather well in the whole plasma, except at the location of the discontinuity, which is replaced by a smooth transition in FLOW. However, it is clear that the two-dimensional solution is coming closer to the one-dimensional one with increasing resolution. Fig. 15 also gives a good feeling for how wide the pedestal is in FLOW equilibria with the modified Bernoulli equation for the parameters used in the present work.

Next, Fig. 16 shows the poloidal field. Excellent agreement is found for all curves in the central region of the plasma. Some differences are seen across the discontinuity (a zoom of the transonic region is shown in the bottom right corner of the figure). This is in part due to the approximation used in the 2D calculations, which replaces the discontinuity with a finite gradient. It is seen that the poloidal field slope becomes a better approximation of the correct one with increasing resolution. However, an overshoot in the maximum value of B_p is left in the high resolution solutions. This is mostly due to numerical reasons, as for each grid the peak decreases with increasing number of iterations. The results shown in Fig. 16 were obtained with the maximum number of iterations used in the present study (10 000 for the high-resolution runs). Some small difference between 1D and 2D results is consistently found in the edge region of the plasma, with the field obtained with the two-dimensional solution being smaller than the field calculated with the one-dimensional solver. It is seen that the error decreases with increasing resolution and with increasing number of iterations on each grid. A convergence study shows that the field approaches the one-dimensional result on the two sides of the discontinuity as the number of iterations and the number of grid points increase (not shown) For the highest resolution run, the error in B_p at the plasma edge is $\lesssim$1.2%.

Finally, the total pressure profile is shown in Fig. 17. Excellent agreement is found in the central region of the plasma and up to the transonic surface. A small error, similar to what seen in Fig. 16 is found in the edge region, where the total pressure calculated with the one-dimensional algorithm is larger than the one obtained with the two-dimensional one. The relative error is $\simeq$1%. As highlighted

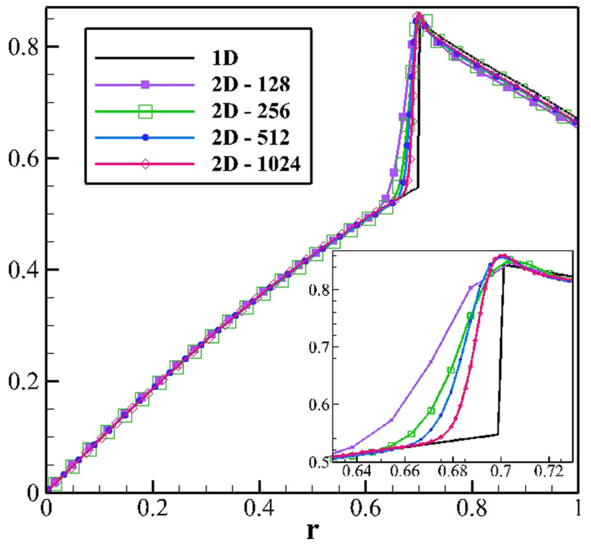

FIG. 16. Poloidal field calculated with the 1D and 2D codes with different resolutions. All results show good agreement, in particular, in the inner region of the plasma. Overshoots (of numerical origin) are seen in the transonic region. The inset in the right-bottom corner of the plot shows details of the profile near the transonic surface.

by the zoom of the transonic region, the accuracy of the two-dimensional solution increases with increasing number of iterations.

Since the purpose of this Appendix is to investigate the convergence properties of the two-dimensional approximate solution, it is worthwhile to examine one more figure, Fig. 18, containing a convergence study of the numerical results shown in the rest of this Appendix. The figure contains three plots, all shown in function of the inverse number of grid points (i.e., of the grid resolution). The "0" point (which would correspond to infinite resolution) is used to show the one-dimensional result (to which a correct two-dimensional approximation must converge). The plot on the left shows the sheath current carried at the transonic singularity. As it was shown in Sec. V (Figs. 7 and 9), a current spike appears across the transonic discontinuity. The toroidal current carried at the transonic surface is responsible for the change in poloidal field. A converging solution will calculate a converging jump in poloidal filed and thus a converging value of the current carried in the singular layer. It is possible to calculate the current in the transonic region as

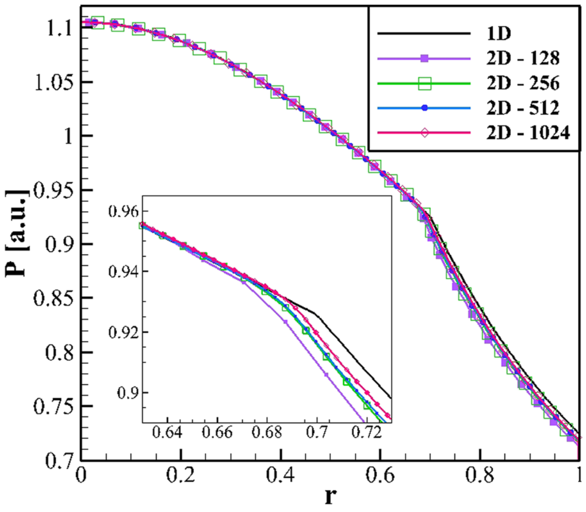

FIG. 17. Total pressure $P = p + B^2/2$ (in arbitrary units) for 1D and 2D solvers. The agreement is excellent inward of the transonic surface, and very good outside the transonic surface, where some small difference appears between the one- and two-dimensional results.

$$I = \int J_\varphi dS = \oint B_p d\ell, \tag{B2}$$

where the surface integral is restricted to the region of the transonic discontinuity and the line integral is taken on the two sides of the same region. The line integral is performed on magnetic surfaces at a location depending on the grid resolution. This is due to the fact that the width of the transonic surface is grid-dependent. Two values of ψ that are approximately located on the two sides of the transonic region are chosen for each grid. The approximation is due to the fact that the transonic region formally extends to the whole plasma, decaying exponentially with increasing distance from the transonic surface, as given by Eq. (A3). For the results shown in Fig. 18, values of ψ 2 e-folds from the transonic surface are used. The choice of the integration surfaces is somewhat arbitrary, but if a consistent choice is made for all grids we expect that the specific choice will not have any qualitative effect on the convergence properties of the quantities shown in Fig. 18. The results in the first plot of Fig. 18 show that the two-dimensional result approaches the one-dimensional one with increasing resolution. The second plot in Fig. 18 (top right) shows the error (in %) of the two-dimensional result for poloidal field value with respect to the one-dimensional value. Two curves are shown, for the values on the two sides of the discontinuity ("In" corresponds to the left of the discontinuity in Figs. 14–17). Both errors decrease with the increasing resolution. The fact that the error for the "In" curve changes sign with the highest resolution considered is simply due to the fact that on this grid the integration surface is slightly to the right of the point where the poloidal field detaches from the one-dimensional value (see Fig. 16). For reference, the actual values of the poloidal field on the two sides of the discontinuity is also shown in Fig. 18 (lower right figure), once more highlighting the increasing accuracy obtained with an increasing number of grid points in the two-dimensional solution.

APPENDIX C: JUMP CONDITIONS IN GAUSS-MODIFIED FORM

It is useful to show explicitly that the Gauss-modified version of the Grad-Shafranov equation satisfies Eq. (8) (continuity of total pressure). We start by rewriting the GS equation including the additional term due to the modification of the Bernoulli equation introduced in Eq. (A2). This is easily accomplished by recalling that the $-\rho H'$ on the right is obtained by replacing the left hand side of the Bernoulli equation (6) with $H(\psi)$ during the derivation of the GS equation. Due to the

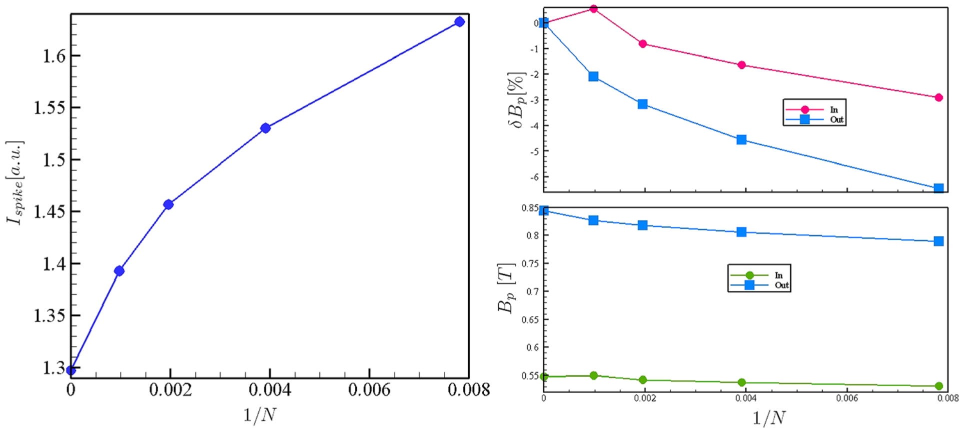

FIG. 18. Convergence of the two-dimensional solution to the one-dimensional one. All plots are in function of the grid size (inversely proportional to the number of grid points). The "0" point corresponds to the one-dimensional solution. Left: Current carried by the transonic surface singularity. Right, top: Error (in %) of the poloidal field on the two sides of the discontinuity; bottom: Value of B_p on the two sides of the discontinuity.

modification to Eq. (6) introduced in Eq. (A2), there will be an extra term containing the derivative of f in the right hand side of the GS equation

$$\nabla\cdot\left[\left(1-\frac{\Phi^2}{\rho}\right)\left(\frac{\nabla\psi}{R^2}\right)\right]=-\frac{B_\varphi}{R}\frac{dF(\psi)}{d\psi}-(\vec{v}\cdot\vec{B})\frac{d\Phi(\psi)}{d\psi}$$
$$-R\rho v_\varphi\frac{d\Omega(\psi)}{d\psi}-\rho\frac{dH(\psi)}{d\psi}$$
$$+\frac{\rho^\gamma}{\gamma-1}\frac{dS}{d\psi}+\rho\frac{\partial f}{\partial\psi} \tag{C1}$$

(keeping in mind that f is a function of ψ and R).

We integrate Eq. (C1) in a layer around the transonic layer, and take the limit for vanishing thickness of the layer, i.e., $\Delta\to\infty$ in Eq. (A3). The derivative of all continuous terms can be ignored with respect to the derivatives of rapidly varying terms (i.e., terms that are discontinuous in a discontinuous equilibrium). The dominant terms give

$$|\nabla\psi|\frac{\partial}{\partial\psi}\left[\left(1-\frac{\Phi^2}{\rho}\right)\frac{|\nabla\psi|}{R^2}\right]=\rho\frac{\partial f}{\partial\psi}, \tag{C2}$$

which we can rewrite as

$$\frac{\partial}{\partial\psi}\left(\frac{|\nabla\psi|^2}{2R^2}\right)-\rho\left[\frac{\partial}{\partial\psi}\left(\frac{\Phi^2|\nabla\psi|^2}{2R^2\rho^2}+f\right)\right]=0. \tag{C3}$$

The second term is replaced using the modified Bernoulli equation (A2), to obtain

$$\frac{\partial}{\partial\psi}\left(\frac{B_\theta^2}{2}\right)-\rho\frac{\partial}{\partial\psi}\left\{-\frac{1}{2}\left[\frac{\Phi(\psi)B_\varphi}{\rho}\right]^2+\frac{1}{2}\cancel{[R\Omega(\psi)]^2}\right.$$
$$\left.-\frac{\gamma}{\gamma-1}S(\psi)\rho^{\gamma-1}+\cancel{H(\psi)}\right\}=0, \tag{C4}$$

in which we can eliminate derivatives of the continuous terms. For convenience, we rewrite the toroidal field as

$$B_\varphi=\frac{1}{R}\frac{F(\psi)+R^2\Phi(\psi)\Omega(\psi)}{1-\Phi^2(\psi)/\rho}\equiv\frac{\mu}{1-\Phi^2/\rho}, \tag{C5}$$

where μ is a continuous function across the discontinuity. For the first term in the curly brackets we then write

$$\rho\frac{\partial}{\partial\psi}\left[\frac{1}{2}\left(\frac{\Phi B_\varphi}{\rho}\right)^2\right]$$
$$=(\rho-\Phi^2)\frac{\partial}{\partial\psi}\left[\frac{\Phi^2}{2}\frac{\mu^2}{(\rho-\Phi^2)^2}\right]+\frac{\partial}{\partial\psi}\left[\frac{\Phi^4}{2}\frac{\mu^2}{(\rho-\Phi^2)^2}\right]$$
$$=\frac{\partial}{\partial\psi}\left[\frac{\Phi^2\mu^2}{(\rho\Phi^2)^2}+\frac{\Phi^4\mu^2}{2(\rho-\Phi^2)^2}\right]=\frac{\partial}{\partial\psi}\left(\frac{B_\varphi^2}{2}\right), \tag{C6}$$

where the last equality holds because we can add a continuous term $\mu^2/2$ inside the derivative. The last term in Eq. (C4) trivially gives

$$\rho\frac{\partial}{\partial\psi}\left[\frac{\gamma}{\gamma-1}S(\psi)\rho^{\gamma-1}\right]=\frac{\partial}{\partial\psi}(S\rho^\gamma)=\frac{\partial p}{\partial\psi}. \tag{C7}$$

Collecting all terms, we are left with the jump condition

$$\frac{\partial}{\partial\psi}\left(p+\frac{B_\varphi^2}{2}+\frac{B_\theta^2}{2}\right)=0, \tag{C8}$$

i.e., continuity of the total pressure. Remarkably, and not surprisingly, the shape of f does not enter the derivation: the only relevant property for f is that it is a rapidly varying function that makes all profiles continuous across the transonic layer.

[1] F. Wagner, G. Becker, K. Behringer, D. Campbell, A. Eberhagen, W. Engelhardt, G. Fussmann, O. Gehre, J. Gernhardt, G. v. Gierke, G. Haas, M. Huang, F. Karger, M. Keilhacker, O. Klüber, M. Kornherr, K. Lackner, G. Lisitano, G. G. Lister, H. M. Mayer, D. Meisel, E. R. Müller, H. Murmann, H. Niedermeyer, W. Poschenrieder, H. Rapp, H. Röhr, F. Schneider, G. Siller, E. Speth, A. Stäbler, K. H. Steuer, G. Venus, O. Vollmer, and Z. Yü, Phys. Rev. Lett. **49**, 1408 (1982).
[2] L. Guazzotto and R. Betti, Phys. Rev. Lett. **107**, 125002 (2011).
[3] L. Guazzotto and R. Betti, Phys. Plasmas **18**, 092509 (2011).
[4] R. Betti and J. P. Freidberg, Phys. Plasmas **7**, 2439 (2000).
[5] L. Guazzotto, R. Betti, J. Manickam, and S. Kaye, Phys. Plasmas **11**, 604 (2004).
[6] A. Manwell, *Tricomi Equation: With Applications to the Theory of Plane Transonic Flow*, Chapman & Hall/CRC Research Notes in Mathematics Series (Pitman Publishing, London, UK, 1979).
[7] H. Ramm, *Fluid Dynamics for the Study of Transonic Flow* (Oxford University Press, Oxford, UK, 1990).

[8] T. H. Moulden, *Fundamentals of Transonic Flow* (Krieger Publishing Company, Malabar, FL, USA, 1990).
[9] S. K. Chakrabarti, *Theory of Transonic Astrophysical Flows* (World Scientific Publishing Company, Inc., Singapore, 1990).
[10] K. G. McClements and M. J. Hole, Phys. Plasmas **17**, 082509 (2010).
[11] A. J. C. Beliën, M. A. Botchev, J. P. Goedbloed, B. van der Holst, and R. Keppens, J. Comput. Phys. **182**, 91 (2002).
[12] J. P. Goedbloed, Phys. Plasmas **19**, 064701 (2012).
[13] R. F. Schmitt, L. Guazzotto, H. Strauss, G. Y. Park, and C.-S. Chang, Phys. Plasmas **18**, 022502 (2011).
[14] E. Hameiri, Phys. Fluids **26**, 230 (1983).
[15] E. Hameiri, Phys. Plasmas **5**, 3270 (1998).
[16] J. P. H. Goedbloed and S. Poedts, *Principles of Magnetohydrodynamics: With Applications to Laboratory and Astrophysical Plasmas* (Cambridge University Press, Cambridge UK, 2004).
[17] L. C. Steinhauer and A. Ishida, Phys. Plasmas **13**, 052513 (2006).
[18] S. Jardin, *Computational Methods in Plasma Physics* (Taylor & Francis, Boca Raton, FL, 2010).
[19] L. Guazzotto and R. Betti, Nucl. Fusion **52**, 114006 (2012).
[20] J. P. Goedbloed and A. Lifschitz, Phys. Plasmas **4**, 3544 (1997).